Journal of Zhejiang University-SCIENCE B (Biomedicine & Biotechnology) in press
www.jzus.zju.edu.cn; www.springer.com/journal/11585
E-mail: jzus_b@zju.edu.cn

Research Article

https://doi.org/10.1631/jzus.B2400340

3D printing-assisted freeze-casting of processed pyritum-doped β-TCP biomimetic scaffold with angiogenesis and bone regeneration capability

Chenxu WEI[1,2,4,*], Zongan LI[3,*], Xiaoyun LIANG[5,*], Yuwei ZHAO[1,2], Xingyu ZHU[1,2], Haibing HUA[4], Guobao CHEN[4], Kunming QIN[6], Zhipeng CHEN[1,2], Changcan SHI[1,2]✉, Feng ZHANG[3]✉, Weidong LI[1,2]✉

[1]*School of Pharmacy, Nanjing University of Chinese Medicine, Nanjing 210023, China*
[2]*Nanjing University of Chinese Medicine, Jiangsu Key Laboratory of Chinese Medicine Processing, Engineering Center of State Ministry of Education for Standardization of Chinese Medicine Processing, Nanjing 210023, China*
[3]*Jiangsu Key Laboratory of 3D Printing Equipment and Manufacturing, School of Electrical and Automation Engineering, Nanjing Normal University, Nanjing 210023, China*
[4]*Jiangyin Hospital Affiliated to Nanjing University of Chinese Medicine, Jiangyin 214400, China*
[5]*School of Pharmacy, Changchun University of Chinese Medicine, Changchun 130117, China*
[6]*School of Pharmacy, Jiangsu Ocean University, Lianyungang 222005, China*

Abstract: Bone repair remains an important target in tissue engineering, making the development of bioactive scaffolds for effective bone defect repair a critical objective. In this study, β-tricalcium phosphate (β-TCP) scaffolds incorporated with processed pyritum decoction (PPD) were fabricated using 3D printing-assisted freeze-casting. The produced composite scaffolds were evaluated for their mechanical strength, physicochemical properties, biocompatibility, in vitro pro-angiogenic activity, and in vivo efficacy in repairing rabbit femoral defects. They not only demonstrated excellent physicochemical properties, enhanced mechanical strength and good biosafety but also significantly promoted the proliferation, migration and aggregation of pro-angiogenic human umbilical vein endothelial cells. In vivo studies revealed that all scaffold groups facilitated osteogenesis at the bone defect site, with the β-TCP scaffolds loaded with PPD markedly enhancing the expression of Notch1, vascular endothelial growth factor, bone morphogenetic protein-2, and osteopontin. Overall, the scaffolds developed in this study exhibited strong angiogenic and osteogenic capabilities both in vitro and in vivo. The incorporation of PPD notably promoted the angiogenic-osteogenic coupling, thereby accelerating bone repair, which suggests that PPD is a promising material for bone repair and that the PPD/β-TCP scaffolds hold great potential as a bone graft alternative.

Key words: Bone defect; Processed pyritum; 3D-printing freeze-casting; Angiogenesis; Bone regeneration; VEGF-Notch1-BMP-2-OPN coupling

unedited

1 Introduction

Each year, millions of people worldwide suffer from painful bone defects and require bone grafts (Giannoudis et al., 2005). The repair of large bone defects caused by trauma, infection, tumor resection, and other

✉ Changcan SHI, cshi@njucm.edu.cn
Feng ZHANG, fengzhan@njnu.edu.cn
Weidong LI, liweidong0801@njucm.edu.cn
[*] The three authors contributed equally to this work
Changcan SHI, https://orcid.org/0000-0003-2416-6278
Feng ZHANG, https://orcid.org/0000-0001-6206-5537
Weidong LI, https://orcid.org/0000-0002-7664-1512

Received July 7, 2024; Revision accepted Sept. 1, 2024;
Crosschecked xxx. xx, 20xx; Published online xxx. xx, 20xx

© Zhejiang University Press 2024

factors remains a major clinical challenge for reconstructive surgeons (Zha et al., 2021; Zhao et al., 2011; Lee et al., 2018; Wang et al., 2023; Zhang et al., 2023). Advances in tissue engineering have provided new options for bone defect repair (Wang et al., 2020; Liu et al., 2023; Maazouz et al., 2020), with artificial bone scaffolds offering advantages such as abundant donor sources, low immune rejection, and personalization while avoiding the risk of donor-transmitted infectious diseases (Qin et al., 2022; Qin et al., 2019; Putra et al., 2022; Qin et al., 2022). However, the physicochemical properties of most artificial bone repair products are inferior in terms of supporting the skeletal structure (Zhang et al., 2019) and they often have low mechanical strength, inadequate osteogenic performance and poor vascularization potential (Li et al., 2020; Zhang et al., 2023).

Processed pyritum, mainly composed of FeS2 (pyrite), is one of the most important traditional Chinese medicines (Shi et al., 2023). Clinical applications have demonstrated that processed pyritum can promote bone reconstruction (Zhu et al., 2018), relieve pain and enrich blood (Shi et al., 2023; Liu et al., 2017). Experimental studies revealed that processed pyritum could promote osteoblast differentiation and osteogenic function (Wang et al., 2021; Xu et al., 2023). Pyritum contains iron, magnesium, calcium, and other beneficial metal elements that are clinically efficient in the recovery of tendons and connecting bones. These metal elements can promote the process of bone vascularization by facilitating the expression of vascular endothelial growth factor (VEGF) and angiogenesis-related genes, along with activating related pathways to regulate bone angiogenesis and by promoting the expression of osteogenesis-related genes and proteins, such as bone morphogenetic protein-2 (BMP-2) and osteopontin (OPN). Iron is the most abundant trace element in the body. Appropriate amounts of iron promote osteoblastogenesis and exhibit a certain antimicrobial activity (Li et al., 2022; Yang et al., 2023). Magnesium contributes to forming an immune microenvironment that promotes osteogenesis and induces the production of anti-inflammatory cytokines and tissue repair factors during the early inflammatory period (Qiao et al., 2021). Furthermore, it affects angiogenesis and mineralization during bone repair (Tao et al., 2023; Qi et al., 2024). Calcium and zinc can induce osteoprogenitor cell differentiation through growth factor signaling pathways or stimulate other processes supporting bone tissue growth (Bai et al., 2023). Zinc supports the proliferation of osteoblasts, increases alkaline phosphatase activity, and also exhibits antimicrobial properties (Wang et al., 2021). The sulfur contained in pyritum inhibits osteoclasts and exerts a positive effect on promoting osteogenesis and vascularization during bone regeneration (Zhou et al., 2022; Zhou et al., 2023). Research has shown that the addition of metal elements to ceramic materials can enhance their mechanical properties to a certain extent (Dong et al., 2022; Putra et al., 2023; Wang et al., 2022) and simultaneously promote the bone angiogenesis and osteogenic coupling processes.

Beta tricalcium phosphate (β-TCP) is a popular bone filling and graft material owing to its chemical composition similar to bone (Wang et al., 2012) and good biocompatibility (Seidenstuecker et al., 2017), excellent biodegradability (Lee et al., 2016), osteoinductivity, and osteoconductivity (Bohner et al., 2020; Ye et al., 2022). In clinical applications (Wang et al., 2013; Hernigou et al., 2017), β-TCP was found to be an ideal bone substitute for treating bone defects. The scaffolds prepared using β-TCP can be resorbed and remodeled into new bone in vivo and produce fewer side effects than autologous bone grafts, leading to less pain to the recipient. Recently, the addition of biologically important metal ions to β-TCP to promote its biological performance has attracted much attention (Yu et al., 2018; Salamanca et al., 2022).

A porous microstructure is critical for the scaffold to promote good osteoinductivity and osteoconductivity. Among the various pore structure fabrication methods, freeze-casting technology has been widely used in the field of preparing bionic controllable biomaterials, such as ceramics and nanomaterials, because of its ease of operation, low cost and environmentally friendly nature, which greatly broadens the applicability of the material (Shao et al., 2020; Chen et al., 2022; Cheng et al., 2017; Li et al., 2024; Deville et al., 2022). In this study, we used 3D printing-assisted freeze-casting technology to develop a bone repair scaffold with improved physicochemical properties. As for the material choice, we added the traditional Chinese medicine processed pyritum decoction (PPD) to β-TCP ceramic. 3D printing templated polydimethylsiloxane (PDMS) mold was prepared according to the biological geometry feature of the recipient. The freeze casting process allowed the formation of biomimetic micropores inside the bulk graft. The two-component PPD/β-TCP was prepared as the material

Unedited

for freeze casting to form the bone repair bio-scaffold. The scaffolds exhibited good mechanical properties, porosity and other beneficial physicochemical properties. Cell experiments indicated that the scaffold was not cytotoxic and exerted pro-angiogenic activity, while the repair of induced femoral defects in New Zealand white rabbits demonstrated the good in vivo bone repair performance of the scaffolds. Regarding the potential repair mechanism, the VEGF-Notch1-BMP-2-OPN angiogenic-osteogenic coupling signaling pathway may be involved. The preparation of bone repair scaffolds with β-TCP loaded with PPD offers a new technical route for the future preparation of scaffolds for bone defect regeneration and repair.

2 Materials and methods

2.1 Preparation and characterization of scaffolds

2.1.1 Experimental materials

β-TCP (particle size of 0.20 μm, biomedical grade) was purchased from Suzhou Ding'an Technology Co., Ltd. (China); processed pyritum (Lot number 201001311) was provided by Kangmei Pharmaceutical Co., Ltd. (China); glycerol (Lot number GY20211107) was purchased from Shandong Ruisheng Pharmaceutical Excipients Co., Ltd. (China); high-glucose Dulbecco's modified Eagle medium (DMEM) was purchased from Bio-Channel Biotechnology Co., Ltd. (China); fetal bovine serum was purchased from Gibco (USA), and cell counting kit-8 (CCK-8) was provided by APExBIO Technology LLC. (USA).

unedited

2.1.2 Preparation of PPD

To prepare PPD, a certain amount of processed pyritum was taken and added with five times the amount of ultrapure water. Subsequently, it was refluxed for extraction for 120 min, filtered, concentrated, passed through a 0.45 μm nylon membrane, and adjusted to a drug content of 10 g/mL. The final solution was stored at 4°C until further use.

The four ion concentrations with the highest PPD content are listed in Table 1.

Table 1 Content of iron, sulfur, calcium, and magnesium in PPD.

Element	Content (mg/mL)
Iron	43.30 ± 0.03
Sulfur	26.60 ± 0.07
Calcium	2.35 ± 0.01
Magnesium	1.80 ± 0.02

All values (n=3) are demonstrated as mean±standard deviation (SD).

2.1.3 Preparation of the scaffolds

The process flow of scaffold preparation is illustrated in Fig. 1a. First, 3.07 g of β-TCP were weighed, followed by the addition of 1 mL of Polyvinyl Alcohol (PVA) solution (8.44 wt %), 300 mg of glycerol, and different volumes of PPD, so that the percentages of processed pyritum were 0%, 5%, and 10%. Ultrapure water was added to reach the same final volumes. The prepared slurry was mixed thoroughly on an adjustable mixer and then injected into the PDMS molds on a freezing platform at −30°C. The PDMS molds were prepared according to the geometry feature of the desired graft using a recently reported method (Zhang et al., 2024). After freeze casting, the molds were demolded, the scaffolds were lyophilized in a freeze-dryer, taken out, and sintered in a muffle furnace at 2°C/min according to the set procedure. The sintering temperatures were set at 1050°C, 1100°C, and 1150°C, respectively, for testing the properties of three different sets of scaffolds.

2.1.4 Mechanical properties of the scaffolds

The mechanical strength of the scaffolds sintered at 1050°C, 1100°C, and 1150°C for 360 min was

measured under a heating rate of 2°C/min. The scaffolds in each group were placed in a biomechanical electric servo testing system (MTS Acumen3, MTS Systems Corporation, USA), and the mechanical strength of the scaffolds under compression was recorded at a compression speed of 1.0 mm/min. The force area of the scaffolds was recorded as S and the maximum force was recorded as F. The mechanical strength was calculated using Eq. (1) to obtain the maximum mechanical strength.

$$P = \frac{F}{S} \qquad (1)$$

Simultaneously, the mechanical strength of each scaffold in the β-TCP, LPPD/β-TCP, and HPPD/β-TCP groups with different amounts of PPD extract at a sintering temperature of 1150°C was determined under the same test conditions.

2.1.5 Properties of the sintered scaffolds

X-ray diffraction analysis of the scaffolds was performed using Cu target Kα radiation, λ = 0.15405 nm, tube voltage = 40 KV, current = 30 mA (Yazdanian et al., 2020), and scanning range = 10°-70°.

The samples were analyzed using a Nicolet iS5 Fourier transform-infrared spectrometer, with a wavenumber range of 400-4000 cm^{-1}, scanning time of 16, and a resolution of 4 cm^{-1}. The measurement was performed at room temperature, and the ambient humidity was < 40%.

For assessing the microscopic surface topography of the scaffolds, the surfaces of the specimens were examined using scanning electron microscopy (S-4800, Hitachi, Ltd., Japan) to characterize the porous microstructure at 10 kV.

Scaffold materials (20 mg) in different groups were dissolved in 500 μL of phosphate-buffered saline (PBS; 0.01 mol/L, pH 7.2-7.4), with ultrapure water as the positive control and 0.01 mol/L PBS (pH 7.2-7.4) as the negative control. After 30 min of water bath at 37°C, 500 μL of 2% red blood cell suspension was added to each tube and mixed. The sample tubes from each group were bathed at 37°C for 60 min and centrifuged at 1000 rpm for 10 min. The supernatant was transferred into a 96-well cell culture plate (80 μL/well), and the optical density (OD) value of each group was measured at 540 nm. The hemolysis rate (HR) was calculated using the following Eq. (2):

$$HR(\%) = \frac{OD_{experimental\ group} - OD_{negative\ group}}{OD_{positive\ group} - OD_{negative\ group}} \times 100 \qquad (2)$$

2.1.6 Shrinkage of the scaffolds

An electronic balance was used to weigh the mass (m) of each scaffold, and a digital vernier caliper was employed to measure the diameter (Φ) and height (h) of each corresponding scaffold. The volume of the scaffold was recorded as V. Before sintering in the muffle furnace, it was recorded as m_1, Φ_1, h_1, and V_1, and the corresponding scaffolds were recorded as m_2, Φ_2, h_2, and V_2 after sintering. Then, the mass shrinkage (ω_m), volume shrinkage (ω_v), transverse shrinkage (ω_x), and vertical shrinkage (ω_y) of the scaffolds were calculated according to the following Eqs. (3)-(5):

$$V = \pi h \left(\frac{\Phi}{2}\right)^2 \qquad (3)$$

$$\omega_m = \frac{m_1 - m_2}{m_1} \times 100\% \ ; \ \omega_v = \frac{V_1 - V_2}{V_1} \times 100\% \qquad (4)$$

$$\omega_x = \frac{\Phi_1 - \Phi_2}{\Phi_1} \times 100\% \ ; \ \omega_y = \frac{h_1 - h_2}{h_1} \times 100\% \qquad (5)$$

unedited

2.1.7 Porosity of the scaffolds

The porosity of the scaffolds was evaluated using Archimedes' s principle (Arahira and Todo, 2016; Kathuria et al., 2009). Briefly, the specific measurement method was as follows: the weight of the dried scaffold was recorded as W_S. The pycnometer was filled with ethanol (95%) and the weight was recorded as W_1. The dry scaffold was added to the pycnometer, and a vacuum pump was used to pump ethanol into the pores inside the scaffold under pressure until no air bubbles were generated in the pycnometer. Ethanol was then added to fill the pycnometer and the weight was recorded as W_2. The scaffold was removed, the pycnometer was weighed, and the ethanol remaining in the bottle was recorded as W_3. The density of ethanol was denoted as ρ_e. The porosity was determined by the following Eq. (6):

$$\text{Porosity}(\%) = \frac{(W_2 - W_3 - W_S)/\rho_e}{(W_1 - W_S)/\rho_e} \times 100 \qquad (6)$$

2.1.8 In vitro degradation and release experiments

In these experiments, the scaffolds were placed into centrifuge tubes containing 5 mL of PBS (pH 7.2-7.4). The tubes were then placed in a constant-temperature water bath shaker at 37 °C for cyclotron oscillation, with a rotating speed of 160 r/min. The scaffolds were then removed and placed in a drying oven on the corresponding days. After drying, the samples were weighed and the cumulative weight loss rates were calculated. Each time a new PBS solution was replaced, the concentrations of calcium and iron in each solution were determined using inductively coupled plasma-mass spectrometry, and the cumulative release was calculated. The pH of the scaffold degradation solution was measured using a pH meter.

unedited

2.2 In vitro cell experiments

Human umbilical vein endothelial cells (HUVECs) were used to assess the cytocompatibility and pro-angiogenic properties of the scaffolds.

2.2.1 Preparation of the scaffold extract

Scaffold extracts were prepared according to the ISO 10993 standard. The scaffolds were soaked in a prepared complete DMEM (high glucose, supplemented with 10% fetal bovine serum, Gibco, Life Technologies Limited, USA), 1% penicillin (100 U/mL), and streptomycin (0.1 mg/mL, Bio-Channel Biotechnology Co., Ltd, China) at a mass volume ratio of 10 g/L and incubated in a thermostatic oscillator (37 °C, 150 r/min). After 48 h, the scaffold extracts were collected and sterile filtered. Samples were stored at 4°C and diluted into different concentrations for subsequent use.

2.2.2 Indirect cell cytotoxicity

HUVECs were seeded into 96-well plates. After 24 h of incubation, the medium was replaced with the scaffold extract for one day. The effects of the scaffold extract on cellular cytotoxicity and cell survival were evaluated by live/dead staining of the co-cultured HUVECs and observation under fluorescence microscopy.

Cell proliferation and viability were detected by the CCK-8 assay. HUVECs were seeded into 96-well plates at a density of 8×10^3/well and cultured for 24 h. Cells were not added to the blank group. The culture medium was changed and the prepared extract was used for the experimental groups, while the complete medium was used for the blank and control groups. Next, four wells were assigned to each group and cultured for one day. The medium was discarded at the labeling time, and 100 μL of CCK-8 solution (1:9 Medium, APExBIO Technology LLC, USA) was added for 1 h. Finally, the absorbance was measured at 450 nm.

2.2.3 Direct cell attachment on the scaffolds

The HUVECs (2×10^6 cells/well) were seeded onto the scaffolds. Incubation for 24 h followed, then the

samples were fixed with a 2.5% glutaraldehyde solution and progressively dehydrated in ethanol. After gold spraying, the samples were observed using a field emission scanning electron microscope (Hitachi Regulus 8100, Japan).

2.2.4 Wound healing experiments

At the back of a 6-well plate, a marker pen was used to draw lines evenly across the wells compared to a straight line, with three lines across each well. HUVECs in the logarithmic growth phase were digested with trypsin, centrifuged and blown into a single-cell suspension with complete DMEM, then inoculated into a 6-well plate at a cell inoculation density of 6.5×10^5 cells/well, with 2 mL of medium per well. The cell culture plate was placed in a cell culture incubator (37 °C, 5% CO_2, and saturated humidity) overnight until the cells were fully adhered and spread over the bottom of the plate at approximately 90% to form a single-cell layer. Using 200-μL yellow pipette tips against a ruler, the fused single-cell layer was scratched perpendicular to the horizontal line on the back of the well plate. While keeping the tip of the pipette perpendicular, three strokes were made per well and the well was washed gently three times with PBS to remove unadhered and deciduous cells. Complete DMEM was added to the blank control group, whereas the drug administration group was added to different groups of scaffold extracts (the concentration of drug administration was sieved according to the CCK-8 experiment). Then, 2 mL of solution was added to each well and the plate was placed in a cell incubator. After 0, 12, and 24 h of drug administration, the cell culture plate was examined under an inverted biomicroscope and photographed at a fixed position using ZEN software. It was ensured that the photographed positions were the same at different times. Eight fixed positions were randomly assigned to each group. The wound area was measured using ImageJ software (National Institutes of Health, Bethesda, MD, USA) to calculate the wound healing rate of each group of HUVECs.

2.2.5 Transwell chamber experiments

The experimental groups and administration concentrations were the same as those in the HUVECs scratch-healing experiment. HUVECs in good growth conditions and in the logarithmic growth phase were digested with trypsin, centrifuged, counted after resuspension in basal DMEM (high glucose), and then diluted into a 5×10^5 cells/mL cell suspension. The blank control group was added with complete DMEM (high glucose), and the drug administration group was added with different groups of scaffold extracts in a volume of 600 μL/well in the lower chamber of Transwell plates. The aforementioned cell suspension was added to the Transwell chamber (chamber membrane pore size 8.0 μm) in a volume of 100 μL/well. The subsequent experimental steps were performed according to the relevant literature (Guo et al., 2022). Cells that migrated to the lower chamber were photographed and counted under an inverted phase-contrast microscope in five randomly selected magnification fields.

2.3 Osteo-promotive effects of scaffolds in vivo

2.3.1 Animal model and scaffold implantation

This study was approved by the Animal Ethics Committee of Nanjing University of Chinese Medicine (No. 202204A075). Male New Zealand white rabbits (3-4 months old) were purchased from Jiangsu Zhenlin Biotechnology Co., Ltd. (Nanjing, China) and maintained in a common facility at the Animal Experiment Center of Nanjing University of Chinese Medicine, license No. SCXK (su) 2021-0011. All rabbits were raised in standard single cages with appropriate bedding, constant temperature, and fed ad libitum (Dai et al., 2018) Sodium pentobarbital (3%) was injected into the ear-margin vein at 30 mg/kg to maintain anesthesia during the entire operation process, and the animals were fixed in the supine position. After washing with physiological saline and iodophor, the skin and fascia were cut open to expose the femurs. A medical electric drill was used to produce a cylindrical cavity with a height of 7 mm and a diameter of 8 mm in the distal femur of rabbits, thus creating a bone defect site. After the scaffolds were sterilized using high-pressure steam and ultraviolet rays, they were implanted into the bone defect by placing them in the cavity. The muscle tissue, fascia, and surface skin were disinfected and sutured layer-by-layer. Each animal received an intramuscular injection of penicillin

Unedited

sodium (400,000 units per day) for the first three days after surgery to prevent infections, and the dietary excretion and mental status of the animals were observed. The following groups were set for the purposes of this study: (I) control group without scaffold implantation; (II) positive group implanted with β-TCP scaffold, (III) LPPD/β-TCP group with 5% PPD and β-TCP scaffold implantation; (IV) HPPD/β-TCP group with 10% PPD and β-TCP scaffold implantation.

The rabbits were sacrificed at 4, 8, and 12 weeks post-operatively by injecting overdosed pentobarbital sodium through the auricular vein. The bones were isolated for microscopic computed tomography scan and histological analysis.

2.3.2 In vivo biosafety tests

Blood samples were collected from male rabbits four weeks after surgery to measure the concentrations of alanine aminotransferase, aspartate aminotransferase, albumin, globulin, total protein, creatinine, blood urea nitrogen (Zhang et al., 2022), and the ratio of albumin to globulin. Simultaneously, the elemental contents of iron, calcium, and phosphorus in the blood samples were determined, and the amount of calcium-phosphorus product was calculated.

The liver, kidney, spleen, and thymus samples of the rabbits were collected after surgery at four weeks to evaluate the biosafety in vivo. After routine embedding, sectioning, hematoxylin and eosin (H&E) staining, images were taken.

2.3.3 Micro-computed tomography (micro-CT)

The animals were sacrificed 4, 8, and 12 weeks after implantation, and femur bone samples were immediately harvested and fixed in 4% paraformaldehyde for further micro-CT analysis (Lee, et al., 2018). The images were reconstructed into three-dimensional images and used to measure new bone volume (μm^3), bone volume density (BV/TV, %), and trabecular separation (Tb.Sp, mm).

2.3.4 Histological and immunohistochemical analysis

Femur samples were taken 4, 8, and 12 weeks after the implantation of scaffolds and fixed with 4% paraformaldehyde for one week. The samples were then decalcified with 10% EDTA until the bone softened, and the specimens were embedded in paraffin wax and sliced. Tissue sections were stained with H&E and Masson's trichrome for histological analysis. Immunohistochemical analysis of the bone samples was performed for selected samples four weeks after scaffold implantation. Immunohistochemical staining was done using antibodies to detect the expression of Notch1, VEGF, and BMP-2, with antibodies against VEGF, BMP-2, and OPN. Semi-quantitative analysis was conducted using Image-Pro Plus software (Media Cybernetics, USA).

2.4 Statistical analysis

All quantitative data were expressed as mean ± standard deviation (SD). Data were analyzed using an independent sample t-test and one-way analysis of variance (ANOVA) for the assessment of statistical significance. Differences were considered statistically significant when the p value was < 0.05.

3 Results

3.1 Preparation and characterization of scaffolds

The scaffold preparation process using 3D-printing freeze-casting technology is shown in Fig. 1a. The scaffold was 7 mm high and 8 mm in diameter. The physical and scanning electron microscopy images of the pure β-TCP scaffold and β-TCP loaded with PPD are shown in Figs. 1b and 1c, respectively. It can be seen that the scaffolds are regular and cylindrical. In the pure β-TCP scaffold group without PPD, the pure white background color of β-TCP can be observed. Meanwhile, the LPPD/β-TCP scaffold and HPPD/β-TCP scaffold

unedited

groups loaded with different doses of processed pyritum extract appear dark red with different color depths. The top and side views of the cylindrical scaffolds reveal the microporous structure of the scaffold. The pore sizes range from 2 to 40 μm, which facilitates cell movement.

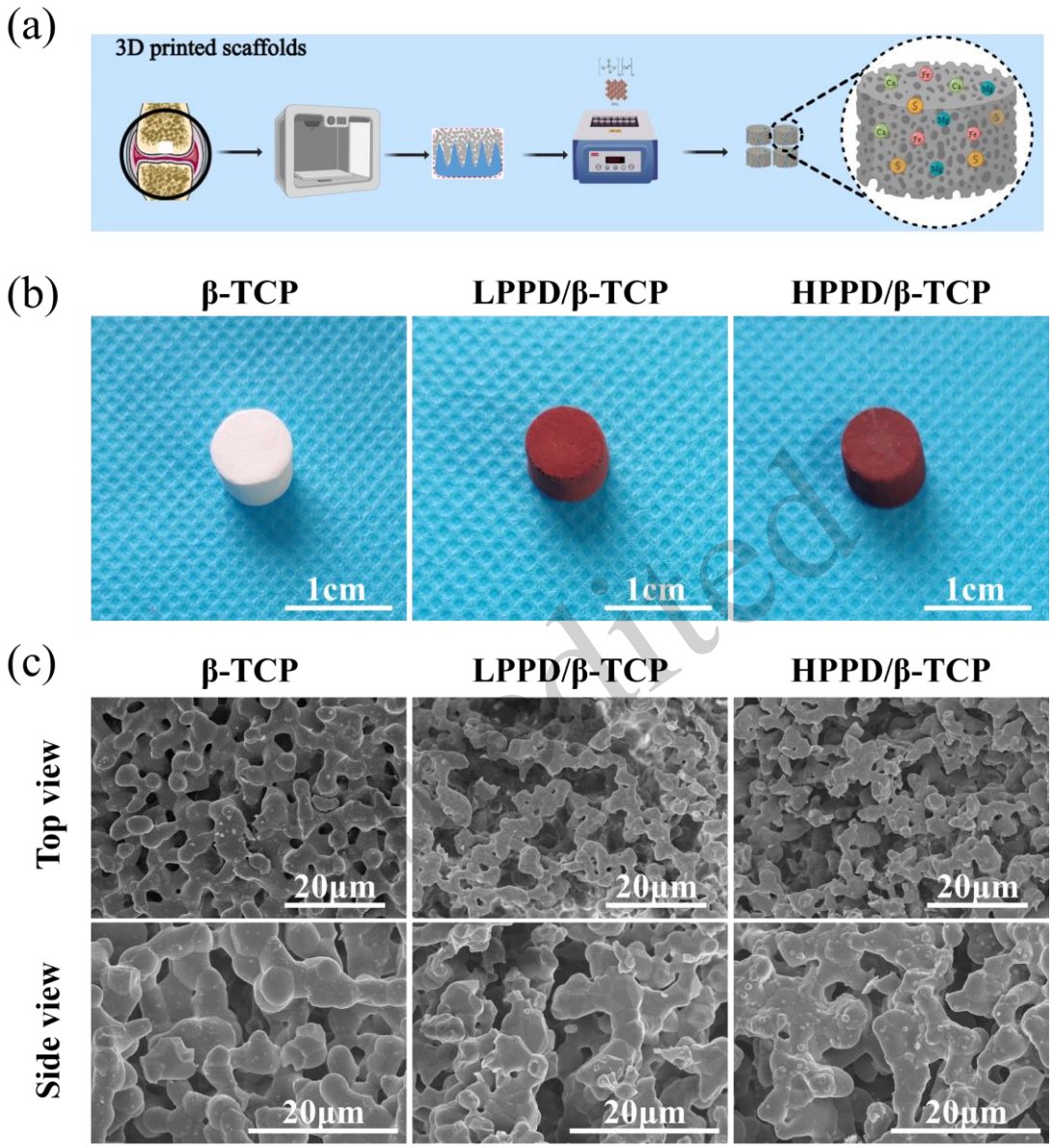

Fig. 1 Preparation and surface morphology of the scaffolds. (a) Preparation process of scaffold using 3D-printing freeze-casting technology. (b) The final formed scaffolds. (c) SEM image of the scaffolds. β-TCP: β-tricalcium phosphate; SEM: Scanning electron microscope; PPD: processed pyritum decoction; LPPD/β-TCP: 5% PPD and β-TCP scaffold; HPPD: 10% PPD and β-TCP scaffold.

Fourier transform-infrared spectroscopy analysis (Fig. 2a) indicated that the scaffolds did not undergo a phase change at this sintering temperature, and no chemical reaction occurred. According to the X-ray diffraction maps (Fig. 2b) of the three sets of scaffolds materials, the main phase of each group of scaffolds was β-TCP phase (PDF#09-0169), among which the samples of LPPD/β-TCP and HPPD/β-TCP scaffolds also contained processed *pyritum* phases (PDF#89-0599). The results are shown in Fig. 2c. When the sintering temperature reached 1150°C, the mechanical strength was greatly improved. Under the same sintering procedure, the me-

chanical strength of the scaffolds after β-TCP drug loading tended to increase. Under the set process conditions of 2°C/min temperature to a sintering temperature of 1150°C and holding time of 360 min, the results of the effect of PPD addition on the mechanical strength of the scaffolds are shown in Fig. 2d. Within a certain dose range, the mechanical strength of the scaffold positively correlated with the PPD dose. Based on the results of mechanical strength measurements, this process was selected for the preparation of the scaffolds. It can be seen in Fig. 2e that the scaffold degradation rate increased over time; by the third week, scaffolds without PPD degraded significantly faster than those in the PPD group. As shown in Fig. 2f, after five weeks of degradation, there was hardly any effect of the solvent pH change during the scaffold degradation process. The release of iron (Fig. 2g) and calcium (Fig. 2h) during degradation shows that after loading with PPD, the release of calcium slowed down, which could have a therapeutic effect on sustained release. As shown in Fig. 2(i), the microporosity of each group was good, distributed in a reasonable range of 68.00% – 82.00%. The scaffolds exhibited good microporous characteristics, as shown in Figs. 2j-2m. HPPD/β-TCP with a high dose of the loaded PPD had the most obvious transverse shrinkage (j), vertical shrinkage (k), mass shrinkage (l), and volume shrinkage (m), which might also contribute to the increase of its mechanical strength after sintering. According to the results of in vitro hemolysis experiments shown in Fig. 2n, the average HR of the three groups of scaffold materials was <5.00%. Referring to the ISO10993-4:2002 standard, this material meets the hemolysis requirements of medical biomaterials.

unedited

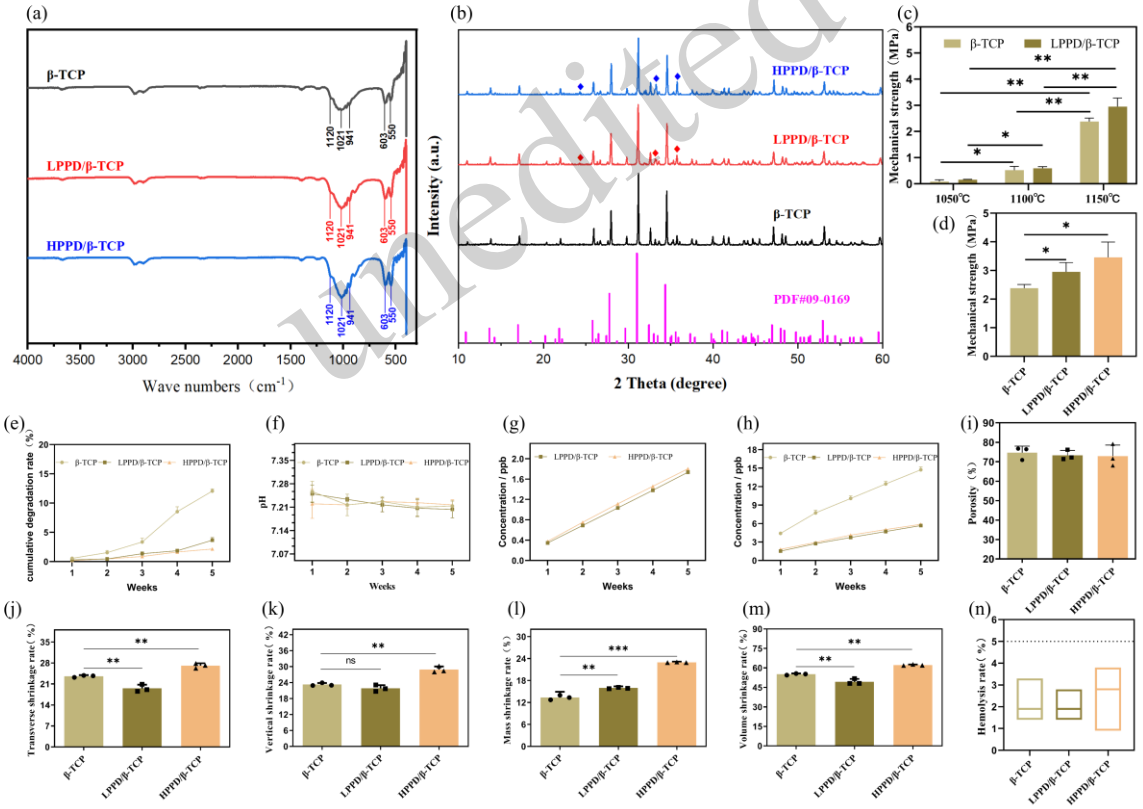

Fig. 2 Characterization of the prepared scaffolds. (a) FT-IR of the scaffold powder. (b) XRD-ray diffraction of the scaffold powder. (c) Mechanical strength test results of each group of scaffolds at different sintering temperatures. (d) Mechanical strength test results of scaffolds with different dosing amounts. (e-h) Degradation and release of scaffolds in vitro; (e): Cumulative degradation rate of scaffolds; (f) Degradation solution pH value; (g): Iron concentration in the degradation solution; (h) Calcium concentration in the degradation solution. (i): The porosity of scaffolds. (j-m) Shrinkage of scaffolds before and after sintering; (j): Transverse shrinkage rate; (k) Vertical shrinkage rate; (l) Mass shrinkage rate; (m) Volume shrinkage rate. (n) In vitro hemolysis experiment. All values (n=3) are demonstrated as mean±standard deviation (SD). *P<0.05; ** P<0.01; *** P<0.001. FT-IR: Fourier Transform Infrared Spectroscopy; β-TCP: β-tricalcium

phosphate; PPD: processed pyritum decoction; LPPD/β-TCP: 5% PPD and β-TCP scaffold; HPPD/β-TCP: 10% PPD and β-TCP scaffold; PBS: phosphate-buffered saline.

3.2 In vitro cell experiments

As shown in Fig. 3a, the cells grew normally in the range of the administered concentrations of scaffold extract, therefore, the scaffolds were found to be safe and reliable. In addition, when the dilution factor was 1000, the proliferative effect of HUVECs in the scaffold extract was the best. The β-TCP scaffold loaded with PPD could significantly promote the proliferation of HUVECs, hence this dilution factor was selected as the concentration of HUVECs for subsequent experiments. As shown in Fig. 3b, the HUVECs in each group showed good survival, normal cell morphology, and normal growth, consistent with the aforementioned CCK-8 results.

The wound healing images and quantitative statistical results for the healing area are presented in Figs 3c and 3d. After 12 and 24 h of administration, relative to the control group, scaffolds in the LPPD/β-TCP and HPPD/β-TCP groups could significantly promote the wound healing of HUVECs. Compared with the β-TCP group, scaffolds in the HPPD/β-TCP group loaded with PPD could significantly promote the wound healing of HUVECs, and within a certain range, the trend of wound healing rate increased in a positive correlation with the dose of PPD.

A schematic of the Transwell chamber migration, Transwell chamber migration assay, and quantitative statistical results are shown in Figs. 3e-3g. After administration, the number of HUVECs penetrating membrane cells increased significantly and the β-TCP scaffolds loaded with PPD promoted the migration of HUVECs. This was confirmed by the aforementioned wound healing experiment, indicating that the scaffold presented a good ability to promote HUVEC migration and healing.

unedited

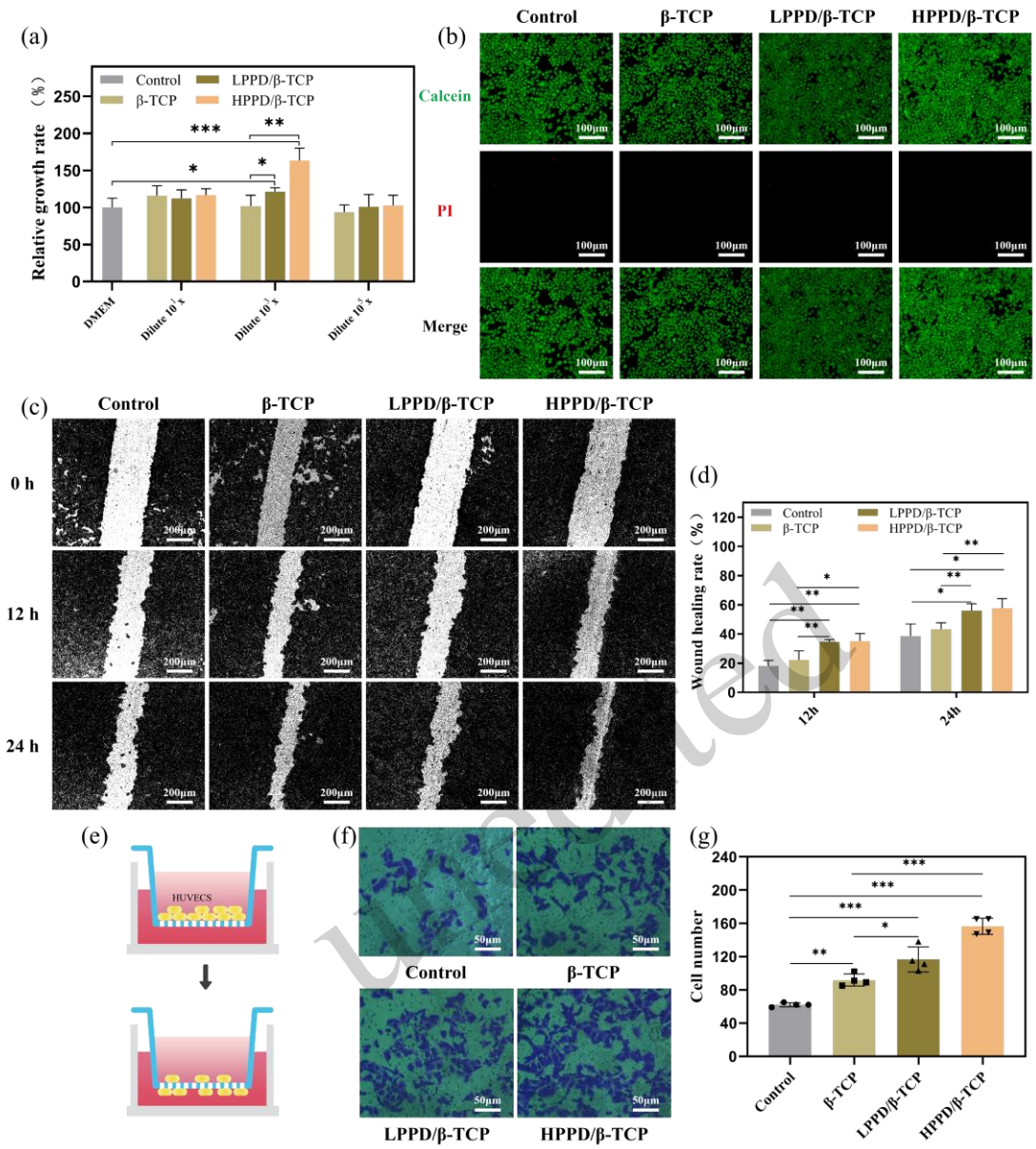

Fig. 3 In vitro cell experiment. (a) 24-h CCK-8 cell proliferation detection. (b) Live/dead staining of HUVECs after culture using scaffold extract for one day. Wound healing experiment (c) and quantitative statistical results of the healing area (d). (e) Schematic of Transwell chamber migration. Transwell chamber migration assay (f) and its quantitative statistical results (g). All values (*n*=4) are demonstrated as mean±standard deviation (SD). *$P<0.05$; ** $P<0.01$; *** $P<0.001$. β-TCP: β-tricalcium phosphate; PPD: processed pyritum decoction; LPPD/β-TCP: 5% PPD and β-TCP scaffold; HPPD/β-TCP: 10% PPD and β-TCP scaffold; DMEM: Dulbecco's modified Eagle medium; PBS: phosphate-buffered saline.

3.3 Osteo-promotive effects of scaffolds in vivo

The results of serological liver and kidney biochemical indexes are shown in Figs. 4a-4h. The main indexes of liver function in all groups of rabbits, such as the alanine aminotransferase (Fig. 4a) and aspartate aminotransferase (Fig. 4b) levels were not significantly increased, and the levels of albumin (Fig. 4c), globulin (Fig. 4d), leukoglobulin ratio (Fig. 4e), and total protein (Fig. 4f) were not significantly decreased. The levels of renal function indicators, such as creatinine (Fig. 4g) and blood urea nitrogen (Fig. 4h) were not significantly increased. These results indicate that the scaffold exhibited good biosafety in vivo.

The results of bone biochemical analyses are shown in Figs. 4i-4l. The data shows that there was no significant difference in the contents of iron (Fig. 4i) and phosphorus (Fig. 4k) among the groups. On the other hand, the contents of calcium (Fig. 4j) and calcium-phosphorus product (Fig. 4l) in the HPPD/β-TCP group were significantly higher than those in the control group. The results of H&E staining of the liver, kidney, spleen, and thymus tissues are shown in Fig. 4m. Pathological analysis revealed that the liver, kidneys, spleen, and thymus were structurally normal without obvious lesions or toxic reactions, indicating that the scaffold had good biocompatibility in vivo.

unedited

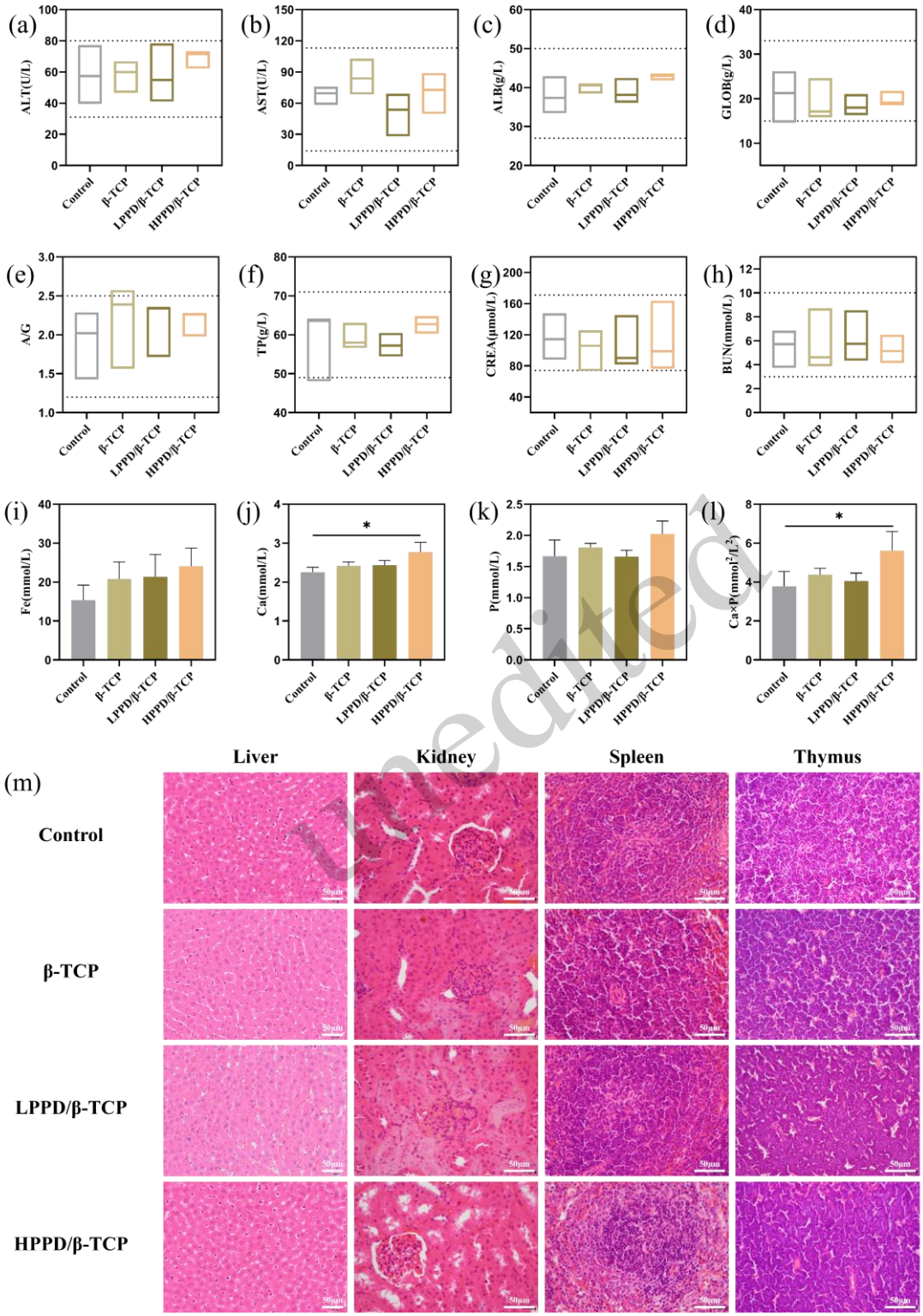

Unedited

Fig. 4 Analysis of serum liver, kidney, and bone biochemical indexes four weeks after operation. (a-h) Biochemical indexes of the liver and kidney. (a): Alanine aminotransferase (ALT); (b) Aspartate aminotransferase (AST); (c) Albumin (ALB); (d) Globulin (GLOB); (e) Albumin/Globulin (A/G); (f) Total protein (TP); (g) Creatinine (CREA); (h) Blood urea nitrogen (BUN). (i-l) Bone biochemical markers. (i) Content of iron; (j) Content of calcium; (k) Content of phosphorus; (l) Calcium-phosphorus product. (m) Organ safety evaluation. All values (*n*=3) are demonstrated as mean±standard deviation

(SD). *$P<0.05$. β-TCP: β-tricalcium phosphate; PPD: processed pyritum decoction; LPPD/β-TCP: 5% PPD and β-TCP scaffold; HPPD/β-TCP: 10% PPD and β-TCP scaffold.

A schematic illustration of our animal study design is shown in Fig. 5a. In the rabbit femoral defect experiment, we analyzed the formation of new bone in the defect area using micro-CT. The result is illustrated in Fig. 5b. Combined with the quantitative analyses of BV (Fig. 5c), BV/TV (Fig. 5d), and Tb.Sp (Fig. 5e), the experiment confirmed that at 4, 8, and 12 weeks postoperatively, there was more bone formation in the area of bone defects in the drug-loaded group than in the pure β-TCP group and more bone formation in the bone defect area in the pure β-TCP group than in the control group. The experimental results confirmed that the scaffold prepared in this study promoted the repair of bone defects to a certain extent, and the addition of traditional Chinese medicine processed pyritum accelerated the bone repair process.

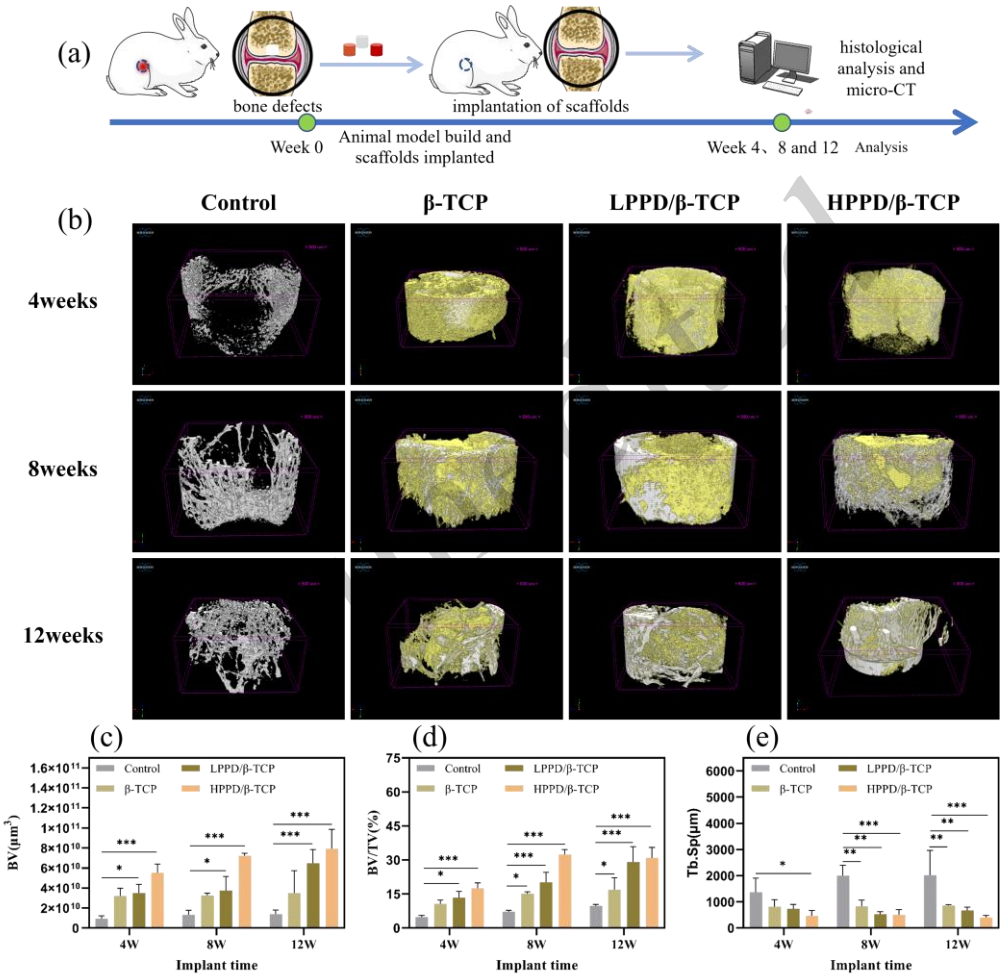

Fig. 5 Gross images and micro-CT analysis results of the repaired bone defects for the four groups at 4, 8, and 12 weeks after surgery. (a) Schematic illustration of the design of the animal study. (b) 3D reconstruction images of the new bone at the defect site on the scaffold. The quantitative data of E BV (c), BV/TV (d), and Tb.Sp (e) for the four groups based on micro-CT images. All values (n=3) are demonstrated as mean±standard deviation (SD). *$P<0.05$; ** $P<0.01$; *** $P<0.001$. β-TCP: β-tricalcium phosphate; PPD: processed pyritum decoction; LPPD/β-TCP: 5% PPD and β-TCP scaffold; HPPD/β-TCP: 10% PPD and β-TCP scaffold; micro-CT: micro-computed tomography.

During the regeneration process, new bone tissue gradually grew toward the central region of the scaffold and entered most of its macropores. In Fig. 6a, the residual scaffold material (black arrow) is visible in the field

of view, except for the control group without the implanted scaffold. The area of the implanted scaffolds exhibit different degrees of trabecular hyperplasia, which are closely arranged and form new bone tissues (red arrow). Osteoblasts and osteoclasts are distributed on the surface of bone trabeculae. With an increase in postoperative time, osteoblasts (gray arrow) gradually increased in number, and those of osteoclasts (blue arrow) decreased. New capillaries (purple arrow) can be observed in the trabecular space and margins, and bone blood vessels continued to form and increase over time. The scaffold in the drug-loaded implantation groups had more bone formation than the β-TCP group, and the pure β-TCP scaffold implantation groups had more bone formation than the control group. Bone formation in the HPPD/β-TCP group with a high PPD dose increased the most; the bone tissue was connected into a large area of new bone tissue, and the separation degree of bone trabecular was reduced. These results were supported by the semi-quantitative histological analysis (H&E) of new bone formation in the implant area (Fig. 6c).

Masson's trichrome staining (Fig. 6b) revealed greater new bone formation in the scaffold implantation groups. The longer the postoperative time, the more new bone tissue was formed. Semi-quantitative histology analysis of new bone formation in the implant area (Fig. 6d) revealed that the LPPD/β-TCP and HPPD/β-TCP groups had a greater increase in new bone formation compared with the control and TCP groups. The scaffold group with a high drug dose showed a significant increase compared with that in the lower dose group. These results followed the same trend as the H&E staining results, and the two results were mutually supportive.

unedited

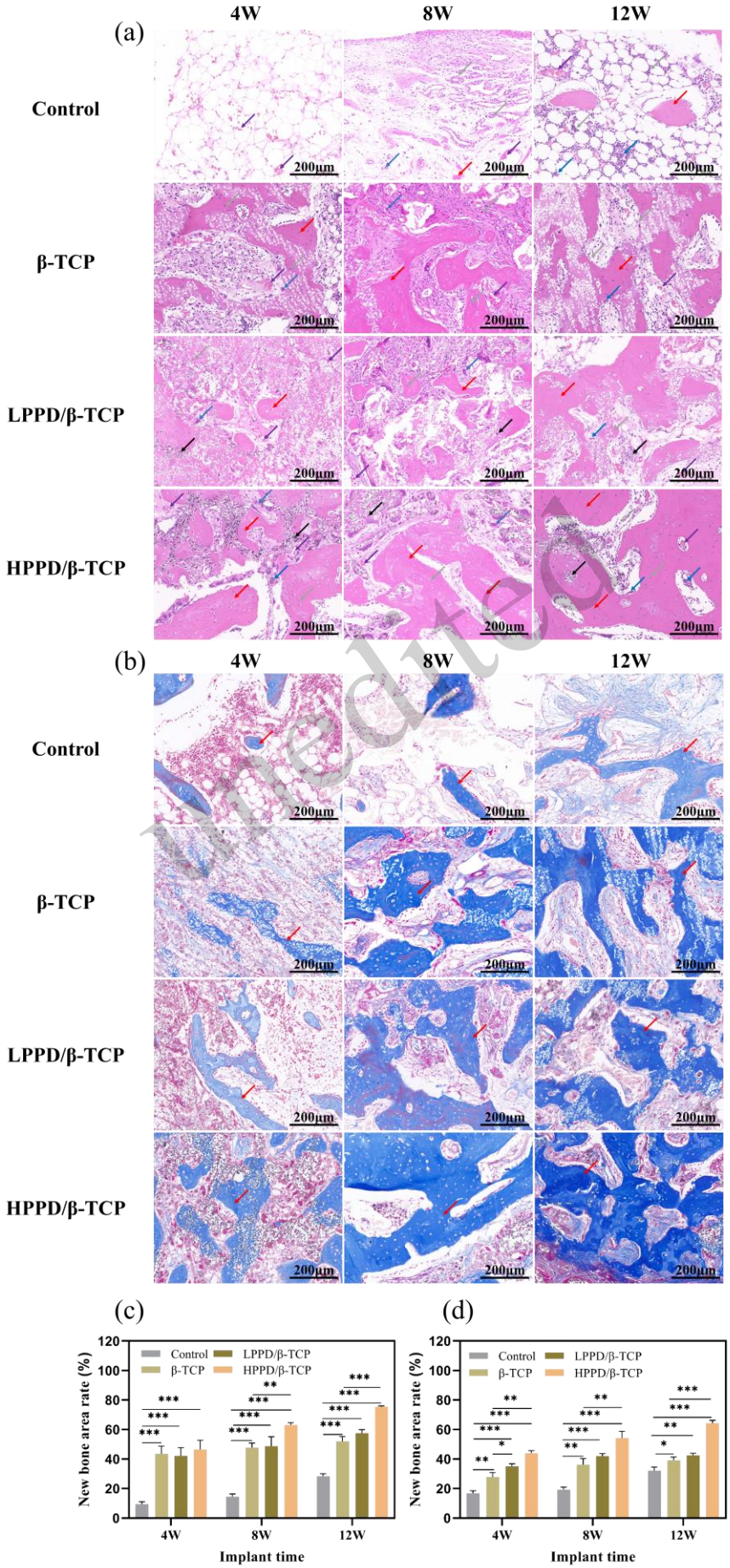
(a)
4W
8W
12W
Control
β-TCP
LPPD/β-TCP
HPPD/β-TCP
200μm
(b)
4W
8W
12W
Control
β-TCP
LPPD/β-TCP
HPPD/β-TCP
200μm
(c)
(d)
Control
β-TCP
LPPD/β-TCP
HPPD/β-TCP
New bone area rate (%)
Implant time
4W
8W
12W

Unedited

Fig. 6 Histomorphometric images and quantitative analysis of the decalcified sections. (a) Representative H&E staining images. (b) Representative Masson staining images. (c-d) Semi-quantitative analysis of new bone tissue: (c) H&E staining; (d) Masson staining (the red arrows represent new osteogenic tissue, the gray arrows represent osteoblasts, the blue arrows represent osteoclasts, the purple arrows represent new capillaries appear, and the black arrows represent undegraded scaffolds). All values (n=3) are demonstrated as mean±standard deviation (SD). *$P<0.05$; ** $P<0.01$; *** $P<0.001$. β-TCP: β-tricalcium phosphate; H&E: hematoxylin and eosin; PPD: processed pyritum decoction; LPPD/β-TCP: 5% PPD and β-TCP scaffold; HPPD/β-TCP: 10% PPD and β-TCP scaffold.

The immunohistochemical staining results for Notch1, VEGF, and BMP-2 is shown in Fig. 7a, and the immunofluorescence staining results of VEGF, BMP-2, and OPN are shown in Fig. 8a. We observed the same trend as that in the results of the aforementioned immunohistochemistry experiments, that is, four weeks after scaffold implantation, the expression of angiogenic and osteogenic factors in the β-TCP group loaded with the traditional Chinese medicine PPD was essentially significantly higher than that in the pure β-TCP group. The semi-quantitative analysis results (Figs. 7b-7d and Figs. 8b-8d) verified the accuracy of the prediction results.

unedited

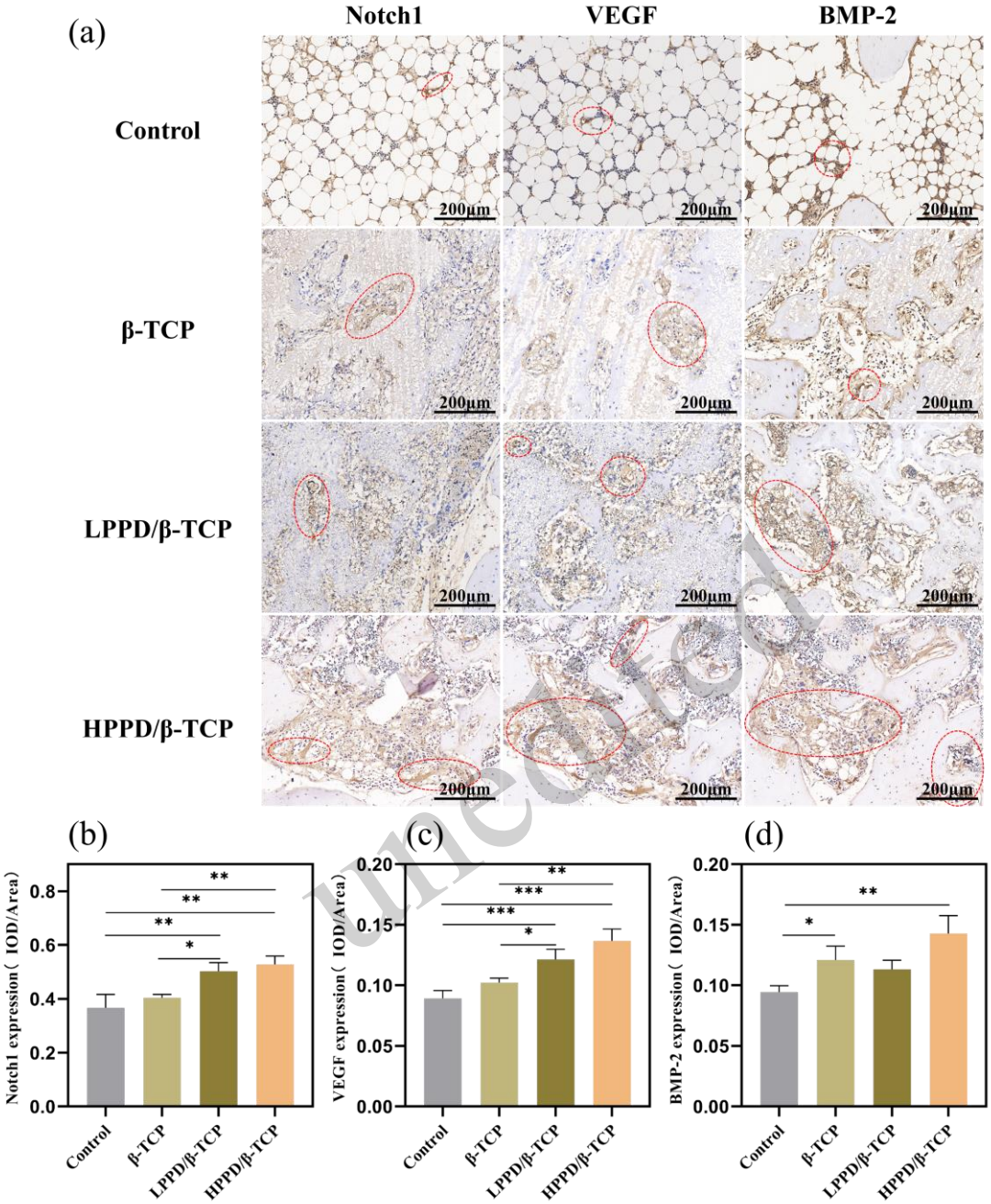

Fig. 7 Immunohistochemical analysis of Notch1, VEGF, and BMP-2 (the red circles represent the respective positive areas). (a) Images of immunohistochemical staining of Notch1, VEGF, and BMP-2 at four weeks. (b-d) Semi-quantitative analysis of new bone formation expressing Notch1, VEGF, and BMP-2 at four weeks: (b) Notch1; (c) VEGF; (d) BMP-2. All values (n=3) are demonstrated as mean±standard deviation (SD). *P<0.05; ** P<0.01; *** P<0.001. β-TCP: β-tricalcium phosphate; PPD: processed pyritum decoction; LPPD/β-TCP: 5% PPD and β-TCP scaffold; HPPD/β-TCP: 10% PPD and β-TCP scaffold; VEGF: vascular endothelial growth factor. BMP-2: bone morphogenetic protein-2.

Unedited

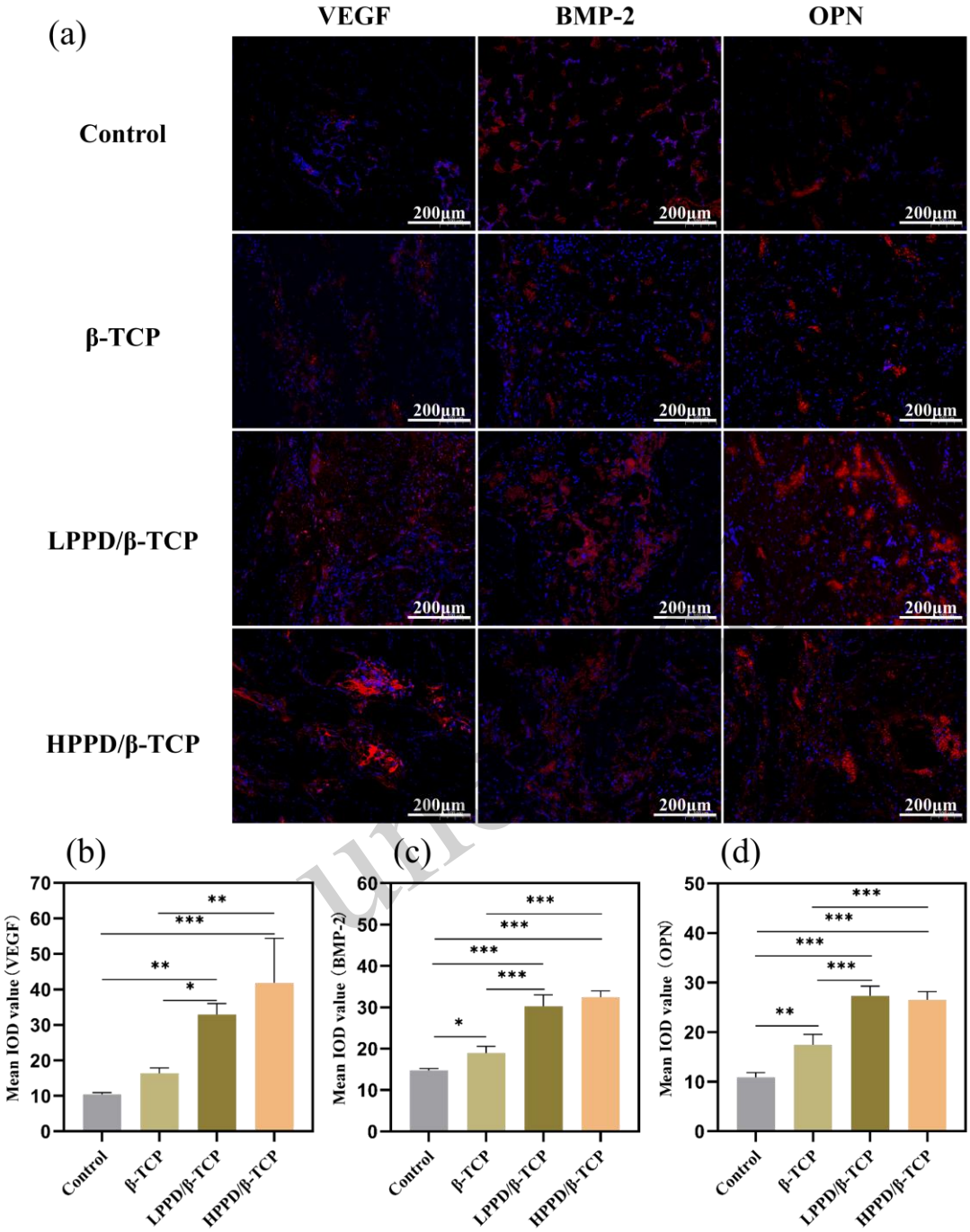

Fig. 8 Immunofluorescence analysis of VEGF, BMP-2, and OPN. (a) Immunofluorescence staining images of VEGF, BMP-2 and OPN at four weeks. (b-d) Semi-quantitative analysis of formation of new bone expressing VEGF, BMP-2, and OPN at four weeks: (b) VEGF; (c) BMP-2; (d) OPN. All values (n=3) are demonstrated as mean±standard deviation (SD). *$P<0.05$; ** $P<0.01$; *** $P<0.001$. β-TCP: β-tricalcium phosphate; PPD: processed pyritum decoction; LPPD/β-TCP: 5% PPD and β-TCP scaffold; HPPD/β-TCP: 10% PPD and β-TCP scaffold; VEGF: vascular endothelial growth factor; BMP-2: bone morphogenetic protein-2; OPN: osteopontin.

4 Discussion

The repair of large bone defects exceeding a certain critical size is an urgent problem in orthopedic clinics. 3D printing technology offers great potential for personalized regenerative repair in bone tissue engineering (Wang et al., 2024). In this study, a novel composite ceramic bone repair scaffold loaded with a traditional Chinese medicine, processed pyritum decoction (PPD), was developed based on 3D-printing freeze-casting technology, and a composite ceramic scaffold promoting the repair of femoral defects in New Zealand white rabbits was prepared by combining PPD with β-TCP, a modern bone repair ceramic material. The fabricated scaffold demonstrated to have good physicochemical properties and biosafety. Moreover, the mechanical properties of the scaffold were significantly enhanced after loading it with PPD, which addresses the shortcomings of insufficient mechanical properties of pure β-TCP and other ceramic materials (Hao et al., 2023; Wang et al., 2024), providing the possibility of repairing the bone defects at the load-bearing bone. It was able to provide good support at the site of load-bearing bone defects rather than rapidly collapsing and fracturing. Based on the available literature (Wang et al., 2021), the mechanical strength of the composite scaffolds meets the clinical requirements for load-bearing bone repair and is at the lower end of the normal range. This level of mechanical strength is more conducive to the degradation and release of the scaffold after implantation as well as cellular infiltration, promoting vascularization, and osteogenesis in the bone microenvironment. Pore structure directly affects osteogenic inducibility (Wu et al., 2024). An appropriate pore structure and porosity directly facilitate the cellular state of the bone microenvironment and cell infiltration, migration, and adhesion (Du et al., 2024), which in turn affect angiogenesis and osteogenesis. For instance, too low porosity of the scaffold hinders the entry of angiogenesis-related cells, while too high porosity in turn impairs the mechanical strength of the scaffold. The porosity of the composite scaffold in this study was in a reasonable range (Joshi et al., 2020), which is conducive to the migration movement of HUVECs and accelerates angiogenesis and osteogenesis during bone defect repair. At the same time, it ensures that the composite scaffold has appropriate mechanical strength.

The bone is a highly vascularized tissue. Angiogenesis is essential for nutrient transport, exchange, and connectivity during bone repair. Several reports have indicated that angiogenesis is closely related to the outcome of bone repair (Guo et al., 2023). VEGF, a key angiogenic factor, acts upstream of Notch1 (Grosso et al., 2023). After scaffold implantation in bone defects, the VEGF receptor is activated and releases VEGF. This stimulates the downstream Notch1 receptor to release Notch1, which in turn promotes bone vascularization. BMP is a member of the transforming growth factor-β superfamily, of which BMP-2 has a highly efficient osteoinductive ability and promotes bone formation. OPN plays an important role in bone matrix mineralization, activates cell aggregation and adhesion, and is closely associated with bone resorption and formation (Zhu et al., 2024). In this study, it was verified by animal experiments that PPD/β-TCP composite scaffolds significantly aid the expression of not only angiogenesis-related factors but also osteogenesis-related proteins through the angiogenesis-osteogenesis coupling of the VEGF-Notch1-BMP-2-OPN pathway. This effect greatly facilitated the process of bone repair in the induced rabbit bone defects.

5 Conclusion

In this work, PPD/β-TCP bone repair scaffolds loaded with a traditional Chinese medicine, processed pyritum decoction (PPD), was successfully prepared and extensively investigated for their biosafety, mechanical properties and ability to facilitate bone repair. The scaffolds exhibited good physicochemical properties such as mechanical strength and biosafety. Cellular and animal experiments demonstrated that the scaffold possessed the dual advantages of significantly promoting angiogenesis and osteogenesis, which in turn promoted bone regeneration and accelerated bone repair. This study provides a new method for the clinical treatment of bone defects. The scaffolds loaded with PPD have great potential for further development in

unedited

clinical settings as a bone repair material.

Data availability statement

All statistical data supporting the findings of this study are available within the paper, and the detailed questionnaire is available from the corresponding author upon reasonable request.

Acknowledgments

This work was jointly supported by the National Science Foundation of China (81373970, 81773902, 81973484, and 32171402); National College Students Innovation and Entrepreneurship Training Program (201810315019); the Postgraduate Research and Practice Innovation Program of Jiangsu Province (SJCX21_0712 and KYCX23_2052) and Jiangyin Science and Technology Innovation Special Fund Project (JY0603A011014230032PB).

Author contributions

Chenxu WEI, Zongan LI, and Xiaoyun LIANG contributed to the conceptualization, methodology, experimental operation, project design, data curation, writing–original draft and writing–review & editing. Yuwei ZHAO, Xingyu ZHU, Haibing HUA, and Guobao CHEN contributed to the experimental operation. Kunming QIN and Zhipeng CHEN contributed to the writing–review & editing. Changcan SHI, Feng ZHANG, and Weidong LI contributed to the resources, project design, conceptualization, supervision, writing–review & editing, project administration, and funding acquisition. All authors have read and approved the final manuscript, and therefore, have full access to all the data in the study and take responsibility for the integrity and security of the data.

Compliance with ethics guidelines

Chenxu WEI, Zongan LI, Xiaoyun LIANG, Yuwei ZHAO, Xingyu ZHU, Haibing HUA, Guobao CHEN, Kunming QIN, Zhipeng CHEN, Changcan SHI, Feng ZHANG, and Weidong LI declare that they have no conflicts of interest.

All institutional and national guidelines for the care and use of laboratory animals were followed. The study was approved by the Nanjing University of Chinese Medicine Animal Ethics Committee (No. 202204A075), China

unedited

References

Arahira T, Todo M, 2016. Variation of mechanical behavior of β-TCP/collagen two phase composite scaffold with mesenchymal stem cell in vitro. *J Mech Behav Biomed Mater*, 61:464-474.
https://doi.org/10.1016/j.jmbbm.2016.04.019

Bai L, Song PR, Su JC, 2023. Bioactive elements manipulate bone regeneration. *Biomater Transl*, 4(4):248-269.
https://doi.org/10.12336/biomatertransl.2023.04.005

Bohner M, Santoni BLG, Döbelin N, 2020. β-tricalcium phosphate for bone substitution: Synthesis and properties. *Acta Biomater*, 113:23-41.
https://doi.org/10.1016/j.actbio.2020.06.022

Chen J, Li YW, Liu SB, et al., 2022. Freeze-casting osteochondral scaffolds: The presence of a nutrient-permeable film between the bone and cartilage defect reduces cartilage regeneration. *Acta Biomater*, 154:168-179.
https://doi.org/10.1016/j.actbio.2022.09.069

Cheng QF, Huang CJ, Tomsia AP, 2017. Freeze Casting for Assembling Bioinspired Structural Materials. *Adv Mater*, 29(45):1703155.
https://doi.org/10.1002/adma.201703155

Dai ZY, Li Y, Yan YG, et al., 2018. Evaluation of the internal fixation effect of nano-calcium-deficient hydroxyapatite/poly-amino acid composite screws for intraarticular fractures in rabbits. *Int J Nanomedicine*, 13:6625-6636.
https://doi.org/10.2147/IJN.S173358

Deville S, Tomsia AP, Meille S, 2022. Complex Composites Built through Freezing. *Acc Chem Res*, 55(11):1492-1502.
https://doi.org/10.1021/acs.accounts.2c00064

Du SR, Huynh T, Lu YZ, et al., 2024. Bioactive polymer composite scaffolds fabricated from 3D printed negative molds enable bone formation and vascularization. *Acta Biomater*, 30: S1742-7061(24)00419-7.
https://doi.org/10.1016/j.actbio.2024.07.038.

Dong J, Lin P, Putra NE, et al., 2022. Extrusion-based additive manufacturing of Mg-Zn/bioceramic composite scaffolds. *Acta Biomater*, 151:628-646.
https://doi.org/10.1016/j.actbio.2022.08.002

Giannoudis PV, Dinopoulos H, Tsiridis E, 2005. Bone substitutes: an update. *Injury*, 36:S20-27.
https://doi.org/10.1016/j.injury.2005.07.029

Grosso A, Lunger A, Burger MG, et al., 2023. VEGF dose controls the coupling of angiogenesis and osteogenesis in engineered bone. *NPJ Regen Med*, 8(1):15-29.
https://doi.org/10.1038/s41536-023-00288-1

Guo JW, Wang FX, Hu Y, et al., 2023. Exosome-based bone-targeting drug delivery alleviates impaired osteoblastic bone formation and bone loss in inflammatory bowel diseases. *Cell Rep Med*, 4(1):100881.
https://doi.org/10.1016/j.xcrm.2022.100881

Guo Y, Chen CL, Zhang SY, et al., 2022. Mediation of mechanically adapted TiCu/TiCuN/CFR-PEEK implants in vascular regeneration to promote bone repair in vitro and in vivo. *J Orthop Translat*, 33:107-119.
https://doi.org/10.1016/j.jot.2022.02.008

Hao SY, Wang MK, Yin ZF, et al., 2023. Microenvironment-targeted strategy steers advanced bone regeneration. *Mater Today Bio*, 22:100741.
https://doi.org/10.1016/j.mtbio.2023.100741

Hernigou P, Dubory A, Pariat J, et al., 2017. Beta-tricalcium phosphate for orthopedic reconstructions as an alternative to autogenous bone graft. *Morphologie*, 101(334):173-179.
https://doi.org/10.1016/j.morpho.2017.03.005

Joshi MK, Lee S, Tiwari AP, et al., 2020. Integrated design and fabrication strategies for biomechanically and biologically functional PLA/β-TCP nanofiber reinforced GelMA scaffold for tissue engineering applications. *Int J Biol Macromol*, 164:976-985.
https://doi.org/10.1016/j.ijbiomac.2020.07.179

Kathuria N, Tripathi A, Kar KK, et al., 2009. Synthesis and characterization of elastic and macroporous chitosan-gelatin cryogels for tissue engineering. *Acta Biomater*, 5(1):406-418.
https://doi.org/10.1016/j.actbio.2008.07.009

Lee DS, Pai Y, Chang S, et al., 2016. Microstructure, physical properties, and bone regeneration effect of the nano-sized β-tricalcium phosphate granules. *Mater Sci Eng C Mater Biol Appl*, 58:971-976.
https://doi.org/10.1016/j.msec.2015.09.047

Lee KG, Lee KS, Kang YJ, et al., 2018. Rabbit Calvarial Defect Model for Customized 3D-Printed Bone Grafts. *Tissue Eng Part C Methods*, 24(5):255-262.
https://doi.org/10.1089/ten.TEC.2017.0474

Li M, Dai XG, Wang MN, et al., 2024. Bioinspired Macroporous Materials of MXene Nanosheets: Ice-Templated Assembly and Multifunctional Applications. *Small Methods*, 8(4):e2300213.
https://doi.org/10.1002/smtd.202300213

Li YL, He J, Ye HX, et al., 2022. Atomic layer deposition of zinc oxide onto 3D porous iron scaffolds for bone repair: in vitro degradation, antibacterial activity and cytocompatibility evaluation. *Rare Met*, 41, 546–558.
https://doi.org/10.1007/s12598-021-01852-8

Li ZW, Du TM, Ruan CS, et al., 2020. Bioinspired mineralized collagen scaffolds for bone tissue engineering. *Bioact Mater*, 6(5):1491-1511.
https://doi.org/10.1016/j.bioactmat.2020.11.004

Liu L, Zhao GH, Gao QQ, et al., 2017. Changes of mineralogical characteristics and osteoblast activities of raw and processed pyrites. *RSC Adv*, 7:28373–28382.
https://doi.org/10.1039/C7RA03970K

Liu XF, Gaihre B, Park S, et al., 2023. 3D-printed scaffolds with 2D hetero-nanostructures and immunomodulatory cytokines provide pro-healing microenvironment for enhanced bone regeneration. *Bioact Mater*, 27:216-230.
https://doi.org/10.1016/j.bioactmat.2023.03.021

Maazouz Y, Rentsch I, Lu B, et al., 2020. In vitro measurement of the chemical changes occurring within β-tricalcium phosphate bone graft substitutes. *Acta Biomater*, 102:440-457.
https://doi.org/10.1016/j.actbio.2019.11.035

Putra NE, Borg KGN, Diaz-Payno PJ, et al., 2022. Additive manufacturing of bioactive and biodegradable porous iron-akermanite composites for bone regeneration. *Acta Biomater*, 148:355-373.
https://doi.org/10.1016/j.actbio.2022.06.009

Putra NE, Leeflang MA, Klimopoulou, M, et al., 2023. Extrusion-based 3D printing of biodegradable, osteogenic, paramagnetic, and porous FeMn-akermanite bone substitutes. *Acta Biomater*, 162:182-198.
https://doi.org/10.1016/j.actbio.2023.03.033

Qi L, Zhao T, Yan JG, et al., 2024. Advances in magnesium-containing bioceramics for bone repair.
Biomater Transl, 5(1): 3-20.
https://doi.org/10.12336/biomatertransl.2024.01.002

Qiao W, Wong KHM, Shen J, et al., 2021. TRPM7 kinase-mediated immunomodulation in macrophage plays a central role in

unedited

magnesium ion-induced bone regeneration. *Nat Commun*, 12(1):2885.
https://doi.org/10.1038/s41467-021-23005-2

Qin Y, Liu AB, Guo H, et al., 2022. Additive manufacturing of Zn-Mg alloy porous scaffolds with enhanced osseointegration: In vitro and in vivo studies. *Acta Biomater*, 145:403-415.
https://doi.org/10.1016/j.actbio.2022.03.055

Qin Y, Wen P, Guo H, et al., 2019. Additive manufacturing of biodegradable metals: Current research status and future perspectives. *Acta Biomater*, 98:3-22.
https://doi.org/10.1016/j.actbio.2019.04.046

Qin Y, Yang HT, Liu AB, et al., 2022. Processing optimization, mechanical properties, corrosion behavior and cytocompatibility of additively manufactured Zn-0.7Li biodegradable metals. *Acta Biomater*, 142:388-401.
https://doi.org/10.1016/j.actbio.2022.01.049

Salamanca E, Pan YH, Sun YS, et al., 2022. Magnesium Modified β-Tricalcium Phosphate Induces Cell Osteogenic Differentiation In Vitro and Bone Regeneration In Vivo. *Int J Mol Sci*, 23(3):1717-1734.
https://doi.org/10.3390/ijms23031717

Seidenstuecker M, Kerr L, Bernstein A, et al., 2017. 3D Powder Printed Bioglass and β-Tricalcium Phosphate Bone Scaffolds. *Materials* (Basel), 11(1):13-33.
https://doi.org/10.3390/ma11010013

Shao GF, Hanaor DAH, Shen XD, et al., 2020. Freeze Casting: From Low-Dimensional Building Blocks to Aligned Porous Structures-A Review of Novel Materials, Methods, and Applications. *Adv Mater*, 32(17):e1907176.
https://doi.org/10.1002/adma.201907176

Shi CC, Yu YT, Wu HJ, et al., 2023. A graphene oxide-loaded processed pyritum composite hydrogel for accelerated bone regeneration via mediation of M2 macrophage polarization. *Mater Today Bio*, 22:100753.
https://doi.org/10.1016/j.mtbio.2023.100753

Tao ZW, Yuan ZY, Zhou D, et al., 2023. Fabrication of magnesium-doped porous polylactic acid microsphere for bone regeneration. *Biomater Transl*, 4(4): 280-290.
https://doi.org/10.12336/biomatertransl.2023.04.007

Wang C, Xue Y, Lin KL, et al., 2012. The enhancement of bone regeneration by a combination of osteoconductivity and osteostimulation using β-$CaSiO_3$/β-$Ca_3(PO4)_2$ composite bioceramics. *Acta Biomater*, 8(1):350-360.
https://doi.org/10.1016/j.actbio.2011.08.019

Wang D, Hou JX, Xia CJ, et al., 2021. Multi-element processed pyritum mixed to β-tricalcium phosphate to obtain a 3D-printed porous scaffold: An option for treatment of bone defects. *Mater Sci Eng C Mater Biol Appl*, 128:112326.
https://doi.org/10.1016/j.msec.2021.112326

Wang J, Wu Y, Li GF, et al., 2024. Engineering Large-Scale Self-Mineralizing Bone Organoids with Bone Matrix-Inspired Hydroxyapatite Hybrid Bioinks. *Adv Mater*, 36(30):e2309875.
https://doi.org/10.1002/adma.202309875

Wang TC, Li WT, Zhang YX, et al., 2023. Bioprinted constructs that simulate nerve-bone crosstalk to improve microenvironment for bone repair. *Bioact Mater*, 27:377-393.
https://doi.org/10.1016/j.bioactmat.2023.02.013

Wang Z, Guo Z, Bai H, et al., 2013. Clinical evaluation of β-TCP in the treatment of lacunar bone defects: a prospective, randomized controlled study. *Mater Sci Eng C Mater Biol Appl*, 33(4):1894-1899.
https://doi.org/10.1016/j.msec.2012.12.041

Wang Z, Wang YC, Yan JQ, et al., 2021. Pharmaceutical electrospinning and 3D printing scaffold design for bone regeneration. *Adv Drug Deliv Rev*, 174:504-534.
https://doi.org/10.1016/j.addr.2021.05.007

Wang ZG, Liu BC, Yin BZ, et al., 2022. Comprehensive review of additively manufactured biodegradable magnesium implants for repairing bone defects from biomechanical and biodegradable perspectives. *Front Chem*, 10:1066103.
https://doi.org/10.3389/fchem.2022.1066103

Wang ZH, Hui AP, Zhao HB, et al., 2020. A Novel 3D-bioprinted Porous Nano Attapulgite Scaffolds with Good Performance for Bone Regeneration. *Int J Nanomedicine*, 15:6945-6960.
https://doi.org/10.2147/IJN.S254094

Wu YH, Liu PX, Feng C, et al., 2024. 3D printing calcium phosphate ceramics with high osteoinductivity through pore architecture optimization. *Acta Biomater*, 11: S1742-7061(24)00380-5.
https://doi.org/10.1016/j.actbio.2024.07.008

Xu L, Xu S, Xiang TY, et al., 2023. A novel peptide hydrogel of metal ion clusters for accelerating bone defect regeneration. *J Control Release*, 353:738-751.
https://doi.org/10.1016/j.jconrel.2022.12.031

unedited

Yang L, Fan L, Lin X, et al., 2023. Pearl Powder Hybrid Bioactive Scaffolds from Microfluidic 3D Printing for Bone Regeneration. *Adv Sci*, 10(34):e2304190.
https://doi.org/10.1002/advs.202304190

Yazdanian M, Tabesh H, Houshmand B, et al., 2020. Fabrication and properties of βTCP/Zeolite/Gelatin scaffold as developed scaffold in bone regeneration: in vitro and in vivo studies. *Biocybern Biomed Eng*, 40(4): 1626-1637.
https://doi.org/10.1016/j.bbe.2020.10.006

Ye XL, Zhang YQ, Liu T, et al., 2022. Beta-tricalcium phosphate enhanced mechanical and biological properties of 3D-printed polyhydroxyalkanoates scaffold for bone tissue engineering. *Int J Biol Macromol*, 209(Pt A):1553-1561.
https://doi.org/10.1016/j.ijbiomac.2022.04.056

Yu W, Li R, Long J, et al., 2018. Use of a three-dimensional printed polylactide-coglycolide/tricalcium phosphate composite scaffold incorporating magnesium powder to enhance bone defect repair in rabbits. *J Orthop Translat*, 16:62-70.
https://doi.org/10.1016/j.jot.2018.07.007

Zha Y, Li YW, Lin TY, et al., 2021. Progenitor cell-derived exosomes endowed with VEGF plasmids enhance osteogenic induction and vascular remodeling in large segmental bone defects. *Theranostics*, 11(1):397-409.
https://doi.org/10.7150/thno.50741

Zhang F, Jia M, Wang JH, et al., 2024. Freeze-Casting of Arbitrary-Shaped Porous Ceramics. *Adv Eng Mater*, 26(12):2301984.
https://doi.org/10.1002/adem.202301984

Zhang HJ, Zhang M, Zhai D, et al., 2023. Polyhedron-Like Biomaterials for Innervated and Vascularized Bone Regeneration. *Adv Mater*, 35(42):e2302716.
https://doi.org/10.1002/adma.202302716

Zhang L, Yang GJ, Johnson BN, et al., 2019. Three-dimensional (3D) printed scaffold and material selection for bone repair. *Acta Biomater*, 84:16-33.
https://doi.org/10.1016/j.actbio.2018.11.039

Zhang YX, Lin T, Meng HY, et al., 2022. 3D gel-printed porous magnesium scaffold coated with dibasic calcium phosphate dihydrate for bone repair in vivo. *J Orthop Translat*, 33:13-23.
https://doi.org/10.1016/j.jot.2021.11.005

Zhang ZB, Liu AB, Fan JD, et al., 2023. A drug-loaded composite coating to improve osteogenic and antibacterial properties of Zn-1Mg porous scaffolds as biodegradable bone implants. *Bioact Mater*, 27:488-504.
https://doi.org/10.1016/j.bioactmat.2023.04.017

Zhao MD, Zhou J, Li XL, et al., 2011. Repair of bone defect with vascularized tissue engineered bone graft seeded with mesenchymal stem cells in rabbits. *Microsurgery*, 31(2):130-137.
https://doi.org/10.1002/micr.20854

Zhou XM, Liu J, Zheng YC, et al., 2022. SM22α-lineage niche cells regulate intramembranous bone regeneration via PDGFRβ-triggered hydrogen sulfide production. *Cell Rep*, 39(5):110750.
https://doi.org/10.1016/j.celrep.2022.110750

Zhou YK, Han CS, Zhu ZL, et al., 2023. M2 exosomes modified by hydrogen sulfide promoted bone regeneration by moesin mediated endocytosis. *Bioact Mater*, 31:192-205.
https://doi.org/10.1016/j.bioactmat.2023.08.006

Zhu XY, Gao QQ, Zhao GH, et al., 2018. Comparison Study of Bone Defect Healing Effect of Raw and Processed Pyritum in Rats. *Biol Trace Elem Res*, 184(1):136-147.
https://doi.org/10.1007/s12011-017-1166-0

Zhu XY, Liu HJ, Mei CM, et al., 2024. A composite hydrogel loaded with the processed pyritum promotes bone repair via stimulate the osteogenic differentiation of BMSCs. *Biomater Adv*, 160:213848.
https://doi.org/10.1016/j.bioadv.2024.213848

unedited